

TUVF: Learning Generalizable Texture UV Radiance Fields

An-Chieh Cheng¹ Xueting Li² Sifei Liu^{2†} Xiaolong Wang^{1†}
¹UC San Diego ²NVIDIA

<https://anjiecheng.me/TUVF>



Figure 1. We propose Texture UV Radiance Fields (TUVF) to render a 3D consistent texture given a 3D object shape input. TUVF provides a category-level texture representation disentangled from 3D shapes. **Top two rows:** TUVF can synthesize realistic textures by training from a collection of single-view images; **Third row:** Given a 3D shape input, we can render different textures on top by using different texture codes; **Bottom row:** We can perform editing on a given texture (adding a flag of France) and apply the same texture on different 3D shapes. All samples are rendered under 1024×1024 resolution; zoom-in is recommended.

Abstract

Textures are a vital aspect of creating visually appealing and realistic 3D models. In this paper, we study the problem of generating high-fidelity texture given shapes of 3D assets, which has been relatively less explored compared with generic 3D shape modeling. Our goal is to facilitate a controllable texture generation process, such that one texture code can correspond to a particular appearance style independent of any input shapes from a category. We introduce Texture UV Radiance Fields (TUVF) that

generate textures in a learnable UV sphere space rather than directly on the 3D shape. This allows the texture to be disentangled from the underlying shape and transferable to other shapes that share the same UV space, i.e., from the same category. We integrate the UV sphere space with the radiance field, which provides a more efficient and accurate representation of textures than traditional texture maps. We perform our experiments on real-world object datasets where we achieve not only realistic synthesis, but also substantial improvements over state-of-the-arts on texture controlling and editing.

† Equal advising.

1. Introduction

3D content creation has attracted a lot of attention given its wide applications in mixed reality, digital twins, filming, and robotics. However, while most current efforts in computer vision and graphics have been spent on 3D shape modeling [6, 80], there is relatively less focus on generating realistic textures [60]. Textures are a key factor in creating immersive experiences in virtual and augmented reality. While 3D shape models are abundant in simulators, animations, video games, industry manufacturing, and synthetic architectures, etc., rendering realistic and 3D consistent texture on these shape models without human efforts (Fig. 1 first two rows) will fundamentally advance the visual quality, functionalities, and experiences.

Given instances of one category, ideally, their textures should be disentangled from their shapes. This can be particularly useful in scenarios where the appearance of an object needs to be changed frequently, but the shape remains the same. For example, it is common in video games to have multiple variations of the same object with different textures to provide visual variety without creating entirely new 3D models. Thus, the synthesis process should also be controllable, i.e., we can apply different textures to the exact shape (Fig. 1 third row) or use the same texture code for different shapes and even edit part of the texture (Fig. 1 bottom row). Supervised learning of such a task is almost unachievable, given the limitation of the training data, i.e., while there are many 3D object shape datasets, the high-fidelity realistic textured 3D mesh is hardly obtainable even with modern physical rendering engines. Recently, the wide utilization of GANs [24, 30] allows training on 3D content creation with only 2D data and supervision [7, 44, 60, 62]. While this alleviates the data and supervision problem, the learned texture representation often highly depends on the input geometry, making the synthesis process less controllable: With the same texture code or specifications, the appearance style of the generated contents changes based on the geometric inputs.

In this paper, we propose a novel texture presentation, Texture UV Radiance Fields (TUVF) for high-quality and disentangled texture generation on any given 3D shape, i.e., a sampled texture code represents a particular appearance style adaptable to different shapes. The key to disentangling the texture from geometry is to generate the texture in a canonical UV sphere space instead of directly on the shape. We train the canonical UV sphere for each category via a Canonical Surface Auto-encoder in a self-supervised manner, so that the correspondence between the UV sphere and the 3D shape is automatically established during training. Such learnable canonical space does not suffer from geometric topology constraints in the mesh representation and can be easily adapted to a continuous radiance field.

To train a texture generator, given an input texture code,

we first encode it with a texture mapping network to a style embedding, which is then projected onto the canonical UV sphere as a textured UV sphere, though another MLP. Given a 3D shape input, we can assign the texture to the corresponding surface coordinates and construct a radiance field with the Canonical Surface Auto-encoder. Given a camera pose and a ray, we can sample the points along the ray and around the object shape surface and render the RGB value using an MLP. In contrast to volumetric rendering [18, 42], constructing the Texture UV Radiance Fields allows efficient rendering and disentangles the texture from the 3D surface. Given the rendered image, instead of using an image reconstruction loss, we apply an adversarial loss where the real dataset is collected from high-quality images from the same category.

We train our model with real-world object datasets [49, 75]. These datasets only provide a 2D collection of single-view images. Fig. 1 visualizes the results of synthesizing 3D consistent texture given a 3D shape. In both cases, our method can provide realistic texture synthesis. More importantly, our method allows complete texture disentanglement from geometry, enabling controllable synthesis and editing (Fig. 1 bottom two rows). With the same shape, we evaluate how diverse the textures can be synthesized. With the same texture, we evaluate how consistently it can be applied across shapes. Our method outperforms previous state-of-the-arts significantly on both metrics.

2. Related work

Neural Radiance Fields. Neural Radiance Fields (NeRFs) have been widely studied on broad applications such as high fidelity novel view synthesis [3, 40, 42, 67] and 3D reconstruction [69, 76, 82]. Following this line of research, the generalizable versions of NeRF are proposed for faster optimization and few-view synthesis [11, 35, 59, 64, 66, 68, 70, 78]. This is related to our work since TUVF is trained in category-level and learns cross-instance correspondence. Instead of learning from reconstruction with multi-view datasets [11, 78], our method leverages GANs for learning from 2D image collections.

From the rendering perspective, instead of performing volumetric rendering [18], more efficient rendering techniques have been applied recently, including surface rendering [45, 77] and rendering with point clouds [73, 74]. Our work relates to the point-based paradigm: Point-Nerf [73] models a volumetric radiance field using a neural point cloud; Neu-Mesh [74] proposes a point-based radiance field using mesh vertices. However, these approaches typically require densely sampled points and are optimized for each scene. In contrast, TUVF only requires sparse points for rendering, and it is generalizable across scenes.

Texture Synthesis on 3D Shapes. Texture synthesis has been an active research area in computer vision and graphics for a long time, with early works focusing on 2D image textures [16, 20, 21, 37, 63] and subsequently expanding to 3D texture synthesis [4, 25, 33, 56, 65]. Recently, learning-based methods [22, 57, 60] combined with differentiable rendering techniques [39, 42] have shown promising results in texture synthesis on 3D shapes by leveraging generative adversarial networks (GANs) [24] and variational autoencoders (VAEs) [32]. These paradigms of work has been applied to textured shape synthesis [7, 23, 52, 53, 62] and scene completion [2, 17]. Motivated by these works, we also adopted GANs for the supervision of a novel representation for 3D texture synthesis. This allows our model to train from a collection of single-view images instead of using multi-view images for training.

To represent texture, there are two main paradigms, including the mesh-based methods [17, 46, 60, 79] and the NeRF-based methods [7, 10, 62, 72]. For example, Texturify [60] is proposed to use 4-RoSy fields [48] for generating textures on a given mesh. However, the texture representation is entangled with the input shape, and the style can change when given different shape inputs. Our approach falls into the NeRF-based category. While the Triplane representation utilized in EpiGRAF [62] also faces a similar problem in structure and style entanglement, the NeuTex approach [72] provides an explicit disentangled representation. However, the NeuTex representation is designed for a single scene. Our TUVF representation disentangles texture from geometry, and it is generalizable across instances which allows transferring the same texture from one shape to another.

Disentanglement of Structure and Style. The disentanglement of structure and style in generative models allows better control and manipulation in the synthesis process. Common approaches to achieve disentanglement include using Autoencoders [28, 32, 34, 38, 41, 51, 55] and GANs [8, 13, 13, 27, 30, 44, 61]. For example, the Swapping Autoencoder [51] learns disentanglement by leveraging network architecture bias and enforcing the texture branch of the network to encode co-occurrent patch statistics across different parts of the image. However, these inductive biases do not ensure full disentanglement, and the definition of disentanglement itself is not clearly defined. In the second paradigm with adversarial training, StyleGAN [30] learns separate mappings for the structure and style of images, allowing for high-quality image synthesis with fine-grained control over image attributes. Recently, CoordGAN [43] shows that it is possible to train GANs so that pixel-wise dense correspondence can automatically emerge. Our work leverages GANs to provide supervision in training, but instead of disentangling texture from 2D structures, we are learning the texture for 3D object shapes.

3. Texture UV Radiance Fields

We introduce a Texture UV Radiance Field (TUVF) that generates a plausible texture UV map conditioned on the shape of a given 3D object. Importantly, semantically corresponding points on different instances across the category are mapped to the same locations on the texture UV map, which inherently enables applications such as texture transfer during inference. As shown in Fig. 2, our texture synthesis pipeline begins with a canonical surface auto-encoder (Sec. 3.1) that builds dense correspondence between a canonical UV sphere and all instances in a category. Such dense correspondence allows us to synthesize textures on a shared canonical UV map using a coordinate-based generator (Sec. 3.2). Finally, since we do not assume known object poses for each instance, we render the generated radiance field (Sec. 3.3) and train the framework with adversarial learning (Sec. 3.4).

3.1. Canonical Surface Auto-encoder

The key intuition of this work is to generate texture on a shape-independent space, where we resort to a learnable UV space containing dense correspondences across different instances in a category. To this end, we learn a canonical surface auto-encoder that maps any point on a canonical UV sphere to a point on an object’s surface [14, 15]. Specifically, given a 3D object O , we first encode its shape into a geometry code $z_{geo} \in R^d$ by an encoder \mathcal{E} [15]. For a point p on the canonical UV sphere, we feed the concatenation of its coordinates X_p and the geometry code into an implicit function f_θ (Fig. 2 red network) to predict the coordinates of the mapped point p' , denoted as $X_{p'}$, on the given object’s surface. We further predict the normal $N_{p'}$ at p' with a separate implicit function g_θ (Fig. 2 blue network). The overall process can be denoted as follows:

$$z_{geo} = \mathcal{E}(O) \tag{1}$$

$$X_{p'} = f_\theta(X_p; z_{geo}), \quad N_{p'} = g_\theta(X_{p'}; z_{geo}) \tag{2}$$

The coordinates and normal of p' are then used for the rendering process discussed in Sec. 3.3.

We use a graph-based point encoder following DGCNN [71] and decoder architecture following [14] for f_θ and g_θ . As proved by [15], correspondences emerge naturally during training, and f_θ and g_θ are trained end-to-end using Chamfer Distance [5] on the surface points and the L2 losses on the indicator grid discussed in Sec. 3.4.

3.2. Texture Feature Generator

The canonical UV sphere defines dense correspondences associated with all instances in a category. Thus, shape-independent textures can be formulated as generating texture UV maps on top of this UV sphere. To this end, we introduce CIPS-UV, an architecture for texture mapping func-

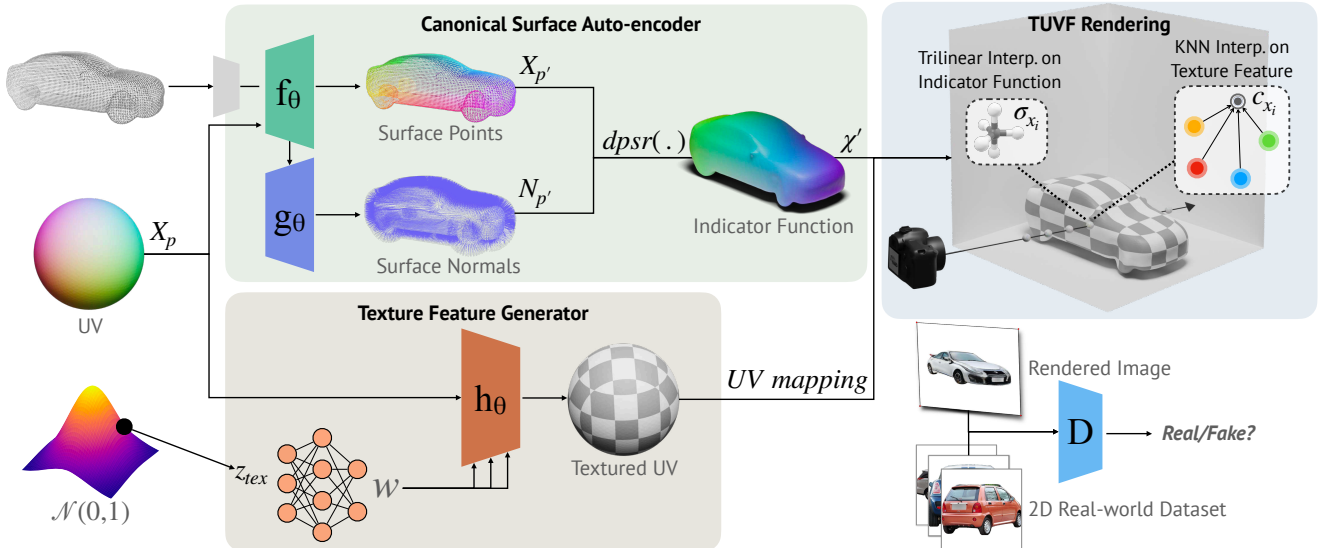


Figure 2. **Method Overview.** We perform two-stage training: (i) We first train the Canonical Surface Auto-encoder with objective Eq. 6, which learns decoders f_θ and g_θ predicting the coordinates and normals for each point on the UV sphere, given an encoded shape. (ii) We then train the Texture Feature Generator h_θ which outputs a textured UV map. We can construct a Texture UV Radiance Field with the outputs from f_θ , g_θ , and h_θ , and render an RGB image as the output. We perform generative adversarial training (Eq. 7) to provide supervision for learning h_θ .

tion h_θ (Fig. 2 green network). Specifically, CIPS-UV takes a 3D point p on the canonical sphere, and a randomly sampled texture style vector $z_{tex} \sim \mathcal{N}(0, 1)$ as inputs and generates the texture feature vector $c_j \in \mathbb{R}^d$ at point p , which are further used for rendering as discussed in Sec. 3.3. The style latent is injected via weight modulation, similar to StyleGAN [30]. We design our h_θ based on the CIPS generator [1], where the style vector z_{tex} is used to modulate features at each layer. This design brings two desired properties. First, combined with the canonical UV sphere, we do not require explicit parameterization, such as unwrapping to 2D. Second, it does not include operators (e.g., spatial convolutions [58], up/downsampling, or self-attentions [81]) that brings interactions between pixels. This is important because nearby UV coordinates may not correspond to exact neighboring surface points in the 3D space. By avoiding these operators, our generator can better preserve the 3D semantic information and produce realistic and diverse textures on the UV sphere.

3.3. Rendering from UV Sphere

Surface rendering is known for its speed, while volume rendering is known for its better visual quality [47]. Similar to [47, 69, 76], we take advantage of both to speed up rendering while preserving the visual quality, i.e., we only render the color of a ray on points near the object’s surface. To identify valid points near the object’s surface, we start by uniformly sampling 256 points along a ray between the near and far planes and computing the density value σ_i (discussed below) for each position x_i . We then compute

the contribution (denoted as w_i) of x_i to the ray radiance as

$$w_i = T_i \cdot \alpha_i \quad (3)$$

$$\alpha_i = 1 - \exp(-\sigma_i \delta), \quad T_i = \exp\left(-\sum_{j=1}^{i-1} \alpha_j \delta_j\right)$$

where δ is the distance between adjacent samples. If $w_i = 0$, then x_i is an invalid sample [26] and will not contribute to the final ray radiance computation. Empirically, we found that sampling only three points for volume rendering is sufficient. It is worth noting that sampling σ_i alone is also fast since the geometry is known in our setting.

Volume Density from Point Clouds. We discuss how to derive a continuous volume density from the Canonical Surface Auto-encoder (Sec. 3.1), which was designed to manipulate discrete points. Given a set of spatial coordinates and their corresponding normal derived from f_θ and g_θ , we use the Poisson Surface Reconstruction algorithm [54] to obtain indicator function values over the 3D grid. We then retrieve the corresponding indicator value $dpsr(x_i)$ for each location x_i via trilinear interpolation. $dpsr(x_i)$ is numerically similar to the signed distance to the surface and can therefore serve as a proxy for density in volume rendering. We follow the formulation from VolSDF [76] to transform the indicator value into density fields σ by:

$$\sigma(x_i) = \frac{1}{\gamma} \cdot \text{Sigmoid}\left(\frac{-dpsr(x_i)}{\gamma}\right) \quad (4)$$

Note that the parameter γ controls the tightness of the density around the surface boundary and is a learnable pa-

parameter in VolSDF. However, since our geometry remains fixed during training, we used a fixed value of $\gamma = 5e^{-4}$.

Point-based Radiance Field. To compute the radiance for a shading point x_i , we query the K nearest surface points $p'_j \in N_K$ in the output space of the Canonical Surface Auto-encoder and obtain their corresponding feature vector $c_{j \in N_K}$ by h_θ . We then use an MLP_F , following [73], to process a pair-wise feature between the shading point x_i and each nearby neighboring point, expressed as $c_{j, x_i} = MLP_F(c_j, p'_j - x_i)$. Next, we apply inverse distance weighting to normalize and fuse these K features into one feature vector c_{x_i} for shading point x_i :

$$c_{x_i} = \sum_{j \in N_K} \frac{\rho_j}{\sum \rho_j} c_{j, x_i}, \quad \text{where } \rho_j = \frac{1}{\|p'_j - x_i\|} \quad (5)$$

Finally, we use another MLP_C to output a final color value for point x_i based on c_{j, x_i} and an optional viewing direction d , denoted $C(x_i) = MLP_C(c_{j, x_i} \oplus d)$. We design MLP_F and MLP_C to be shared across all points, i.e., as implicit functions, so that they do not encode local geometry information.

3.4. Generative Adversarial Training

Patch-based Discriminator. NeRF rendering is expressive but can be computationally expensive regarding time and memory resources when synthesizing high-resolution images. For GAN-based generative NeRFs, using 2D convolutional discriminators that require entire images as inputs further exacerbates this challenge. Thus, in our work, we adopt the efficient and stable patch-discriminator proposed in [62]. During training, we sample patches starting from a minimal scale, covering the entire image in low resolution. As the scale gradually grows, the patch becomes high-resolution image crops. This approach allows the generator to learn progressively and, therefore, stabilizes training. As our rendering process is relatively lightweight (see Section 3.3), we use larger patches (128×128) than those used in [62] (64×64), which brings better quality.

Training objectives. We train the Canonical Surface Auto-encoder (Sec. 3.1) and the Texture Generator (Sec. 3.2) in separate stages. In stage-1, we adopt a Chamfer Distance between the output and input point sets, and a L2 loss to learn the mapping $dpsr(\cdot)$ between points and volume density, as aforementioned:

$$L_{CSAE} = L_{CD}(p, p'_i) + L_{DPSR} \| \chi' - \chi \| \quad (6)$$

where (χ', χ) denotes the predicted and ground truth indicator function (see details in [54]). In stage-2, with \mathbb{R} denotes rendering, we enforce a non-saturating GAN loss with R1

regularization to train the texture generator [30, 62]:

$$L_{GAN} = E_{z_{tex} \sim p_G} [f(D(\mathbb{R}(h_\theta(z_{tex}, X_p))))] \quad (7) \\ + E_{I_{real} \sim p_D} [f(-D(I_{real}) + \lambda \|\Delta D(I_{real})\|^2)], \\ \text{where } f(u) = -\log(1 + \exp(-u)).$$

Data Augmentations and Blur. Direct applying the discriminator fails to synthesize reasonable textures since there exists a geometric distribution shift exists bet collection and rendered 2D images. Therefore, following [7, 62], we apply Adaptive Discriminator Augmentation (ADA) [29] to transform both real and fake image crops before they enter the discriminator. Specifically, we use geometric transformations, such as random translation, random scaling, and random anisotropic filtering. However, we disable color transforms in ADA as they harm the generation process and result in undesired textures.

In addition to ADA, we also blur the image crops, following [7, 62]. However, since we use larger patch sizes, we employ a stronger initial blur sigma (i.e., 60) and a slower decay schedule, where the image stops blurring after the discriminator has seen 5×10^6 images.

4. Experiments

4.1. Dataset

We utilize 3D shape geometry from the ShapeNet dataset’s ”chair” and ”car” categories [9]. For the 2D car dataset, we employ the Compcars dataset [75], while for the 2D chair dataset, we use the Photoshape dataset [50], which contains chair images gathered from image search engines. Notably, the chair category includes subsets with significantly different topologies, such as lounges and bean chairs, where finding a clear correspondence may be challenging even for humans. Consequently, we evaluate our model and the baselines’ performance on the ”straight chair” category, one of the largest subsets in the chair dataset. To guarantee fair comparisons, we follow Texturify’s approach [60], splitting the 1,256 car shapes into 956 for training and 300 for testing. We apply the same split within the ”straight chair” subset for the chair experiment, yielding 450 training shapes and 150 testing shapes.

4.2. Baselines

Mesh-based approaches. Texturify [60] is a state-of-the-art prior work on texture synthesis. They proposed using a 4-rosy field as a better representation for meshes. TexFields [46], SPSG [17], LTG [79], and EG3D-Mesh [7] are all mesh-based baselines. These baselines follow a similar framework, where the texture generators are conditioned on a certain shape geometry condition. The biggest difference among these methods is that they use different representations. Specifically, the TexFields [46] uses a global implicit



Figure 3. Texture synthesis results. Our method achieves much more realistic, high-fidelity, and diverse 3D consistent textures compared to previous approaches. Each column also presents results generated using the same texture code. Texturify [60] and EpiGRAF [62] both have *entangled* texture and geometry representations, which occasionally result in identical global colors or similar local details, despite having different texture codes. Samples are visualized under 1024×1024 resolution; zoom-in is recommended.

function to predict texture for mesh, and SPSG [17] uses 3D convolution networks to predict voxels for textures. EG3D-Mesh [7] uses the triplane representation in EG3D [7] to predict the face colors for a given mesh. Note that all baselines require explicit geometry encoding for texture synthesis. On the other hand, our method relies on correspondence and does not directly condition texture on a given geometry. Furthermore, our learned dense surface correspondence allows for direct texture transfer. We also compare with a concurrent work, Text2Tex [12], which proposes an instance-specific approach for texture synthesis using a pre-trained diffusion model.

NeRF-based approach. We also evaluate our method against a NeRF-based approach, EpiGRAF [62], which is a state-of-the-art 3D GAN that employs a tri-plane representation and a patch-based discriminator. To modify EpiGRAF into a texture generator for radiance fields, we fol-

low TexFields [46] and use a point cloud encoder to encode geometry information into EpiGRAF’s style-based triplane generator. To ensure a fair comparison, we employ the same training pipeline (e.g., the architecture design and hyperparameters) for EpiGRAF [62] and our method.

4.3. Evaluation Metrics

FID and KID. We evaluate our method using standard GAN image quality and diversity metrics, specifically the Fréchet Inception Distance (FID) and Kernel Inception Distance (KID) scores. We follow Texturify’s approach in all experiments, training on 512×512 resolution images. For evaluation, we follow [60] by rendering images at a resolution of 512×512 and subsequently downsampling to 256×256 for assessment. We employ 4 random views and 4 random texture codes for all evaluations, incorporating all available real-world images in the FID/KID calculations.

Method	FID ↓	KID ↓	LPIPS _g ↑	LPIPS _t ↓
TexFields [46]	177.15	17.14	-	-
LTG [79]	70.06	5.72	-	-
EG3D-Mesh [7]	83.11	5.95	-	-
Text2Tex [12] [†]	46.91	4.35	-	-
Texturify [60]	59.55	4.97	9.75	2.46
EpiGRAF [62]	89.64	6.73	4.26	2.34
TUVF (ours)	41.79	2.95	15.87	1.95

Table 1. Comparison on CompCars dataset. The symbol “[†]” denotes an instance-specific approach, whereas the remaining methods employ category-wise training. Our method significantly improves over all previous methods on all metrics. KID is multiplied by 10^2 .

LPIPS_g and LPIPS_t. In addition to FID and KID, we employ two additional metrics to evaluate our model’s ability to disentangle geometry and texture. The first metric, LPIPS_g, is calculated by generating 10 random latent codes for each shape in the test set and measuring the diversity of the synthesized samples. If the model struggles to disentangle, the generated samples may appear similar, leading to a lower LPIPS score. For the second metric, LPIPS_t, we measure the semantic consistency after texture swapping. Specifically, we randomly sample 4 latent codes and transfer them among 100 test shapes. If a model successfully disentangles geometry and texture, all samples with the same texture code should appear visually similar, resulting in a lower LPIPS score.

4.4. Results

Canonical Surface Auto-encoder. To the best of our knowledge, our work represents the first attempt to explore joint end-to-end canonical point auto-encoder [15] and surface learning [54]. A key concern is the smoothness of the learned correspondence and the reconstructed surface, which directly impacts the texture synthesis results. We reconstruct the mesh using the predicted indicator function χ' , and without requiring any proxy function (such as nearest neighbor search based on L2 distance), dense surface correspondence is readily obtained. As a result of the Poisson surface reconstruction, P'_j , which holds the correspondence, naturally lies on the surface. In Fig. 4, we showcase that our reconstructed surface is indeed smooth and that the correspondence is both dense and smooth as well.

Quantitative Texture Synthesis Results. We show the quantitative results of the CompCars dataset in Table 1 and the results of the Photoshape dataset in Table 3. For the CompCars dataset, we achieve significant improvements over all the metrics. For the Photoshape dataset, while our approach is slightly worse than Texturify in FID and KID, as for the fidelity metrics, we obtain much better results on controllable synthesis. We further conduct a user study to

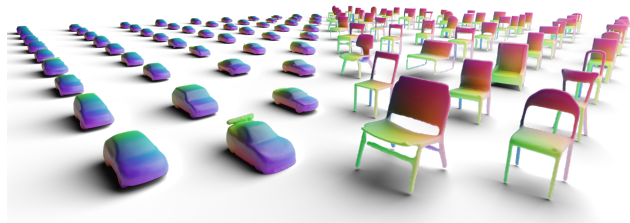


Figure 4. Visualization of the results from the Canonical Surface Auto-encoder. The color map indicates the correspondence map between each instance and the UV sphere.

Dataset	Metric	Texturify ↑	EpiGRAF ↑
CompCars	General	82.40%	85.60%
	Transfer	75.20%	78.40%
Photoshape	General	74.40%	80.00%
	Transfer	70.40%	75.20%

Table 2. Percentage of users who favored our method over the baselines in a user study with 125 responses.

Method	FID ↓	KID ↓	LPIPS _g ↑	LPIPS _t ↓
Texturify [60]	45.92	2.61	6.74	2.89
EpiGRAF [62]	65.62	4.20	7.00	3.14
TUVF (ours)	51.29	2.98	14.93	2.55

Table 3. Comparison on Photoshape dataset. While our method has slightly larger FID and KID compared to Texturify [60], we achieve significantly better results in controllable synthesis. KID is multiplied by 10^2 .

evaluate the texture quality. Two metrics are considered: (1) General: The users compare random renders from baselines and our method, choosing the most realistic and high-fidelity method. (2) Transfer: The users compare three random renders with the same texture code, selecting the most consistent one across shapes. We show the user study results in Table 2.

Qualitative Texture Synthesis Results. We show our qualitative results for texture synthesis in Fig. 3, which confirms that textures generated by our approach are more visually appealing, realistic, and diverse. EpiGRAF suffers from the redundancy of triplane representation, leading to less sharp results. Our proposed method also shows better diversity and disentanglement than Texturify and EpiGRAF. We also show texture transfer results in Fig. 5, where Texturify and EpiGRAF failed to transfer the texture on some of the samples.

Editing Results. Our approach not only achieves disentanglement but also enables image editing. This is made possible because our disentanglement approach allows direct editing of any rendered image by modifying its texture,

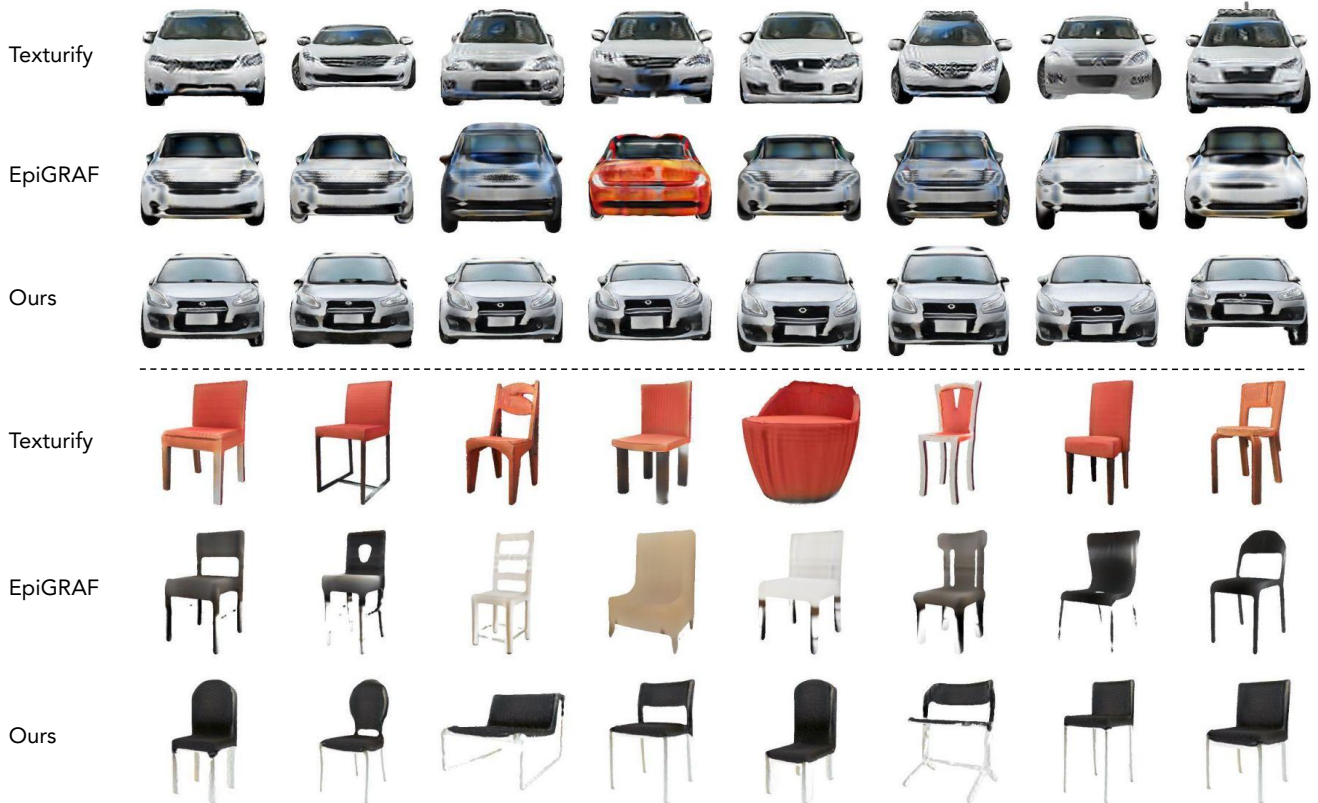


Figure 5. Texture transfer results with models trained with the CompCars (first row) and Photoshape (second row) dataset. Each approach applies the same texture code to synthesize textures on different input shapes. Our method can obtain results with consistent textures across all shapes, while previous approaches output different styles on different object shapes even using the same texture code.

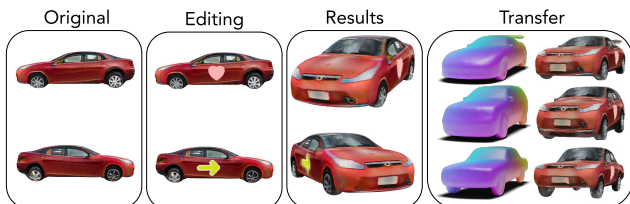


Figure 6. Texture Editing. Given a synthesized texture, one can directly operate on the rendered view to edit the texture. By fine-tuning the edited image through back-propagation to the texture feature, we can obtain an edited texture that is 3D consistent across different views. This edited texture feature further be transferred among different shapes.

such as through drawing or painting. Thanks to the disentanglement, the radiance field is independent of the density condition, and we can directly fine-tune the UV texture features with sparse views without hurting 3D consistency. As shown in Fig. 6, given an edited sample of an image, we can fine-tune the texture representation in a 3D consistent way.

Ablation Study on Texture Generator’s Architecture.

We conducted an ablation study on different texture generator architectures using the CompCars dataset. Two ar-

Architecture	FID ↓	KID ($\times 10^{-2}$) ↓
CIPS-2D [1]	148.09	13.38
StyleGAN2 [31]	103.62	7.89
CIPS-UV (<i>ours</i>)	41.79	2.95

Table 4. Ablation Study over different texture generator architectures. Evaluated on the CompCars dataset.

chitectures were considered: CIPS-2D and StyleGAN2, the former being the same as the one proposed in [1], and the latter being a popular choice for both 2D and 3D GANs. Since the input to both generators is in 3D (i.e., sphere coordinates), an equirectangular projection was first performed to transform the coordinates into 2D. We show the results in Table 4, where CIPS-2D suffers from the explicit parameterization of unwrapping 3D to 2D. Similarly, StyleGAN2 suffers from pixel-wise interaction operators that degrade its performance as well. In contrast, our proposed generator design avoids explicit parameterization and operators that bring interactions between pixels. By preserving 3D semantic information, our generator produces realistic and diverse textures on the UV sphere.

5. Conclusion

In this paper, we present Texture UV Radiance Fields that allow for the creation of textures that can be applied to any input object shape, providing a flexible and controllable way to generate high-quality textures. The key idea is to generate textures in a learnable UV sphere space that is independent of shape geometry and also compact and efficient as a surface representation. Specifically, we leverage the UV sphere space with a continuous radiance field, so that the entire pipeline can be supervised by an adversarial loss on top of rendered images. We achieve not only high-quality and realistic texture synthesis but also substantial improvements over state-of-the-art approaches to texture swapping and editing applications. Specifically, we are able to generate consistent textures over different object shapes while previous approaches fail. With the same object shape, we can generate more diverse textures compared to previous state-of-the-arts.

References

- [1] Ivan Anokhin, Kirill Demochkin, Taras Khakhulin, Gleb Sterkin, Victor Lempitsky, and Denis Korzhenkov. Image generators with conditionally-independent pixel synthesis. In *CVPR*, pages 14278–14287, 2021.
- [2] Dejan Azinović, Ricardo Martin-Brualla, Dan B Goldman, Matthias Nießner, and Justus Thies. Neural rgb-d surface reconstruction. In *CVPR*, pages 6290–6301, 2022.
- [3] Jonathan T Barron, Ben Mildenhall, Matthew Tancik, Peter Hedman, Ricardo Martin-Brualla, and Pratul P Srinivasan. Mip-nerf: A multiscale representation for anti-aliasing neural radiance fields. In *ICCV*, pages 5855–5864, 2021.
- [4] Pravin Bhat, Stephen Ingram, and Greg Turk. Geometric texture synthesis by example. In *SGP*, pages 41–44, 2004.
- [5] Gunilla Borgefors. Hierarchical chamfer matching: A parametric edge matching algorithm. *PAMI*, 10(6):849–865, 1988.
- [6] Rohan Chabra, Jan E Lenssen, Eddy Ilg, Tanner Schmidt, Julian Straub, Steven Lovegrove, and Richard Newcombe. Deep local shapes: Learning local sdf priors for detailed 3d reconstruction. In *ECCV*, pages 608–625. Springer, 2020.
- [7] Eric R Chan, Connor Z Lin, Matthew A Chan, Koki Nagano, Boxiao Pan, Shalini De Mello, Orazio Gallo, Leonidas J Guibas, Jonathan Tremblay, Sameh Khamis, et al. Efficient geometry-aware 3d generative adversarial networks. In *CVPR*, pages 16123–16133, 2022.
- [8] Eric R Chan, Marco Monteiro, Petr Kellnhofer, Jiajun Wu, and Gordon Wetzstein. pi-gan: Periodic implicit generative adversarial networks for 3d-aware image synthesis. In *CVPR*, pages 5799–5809, 2021.
- [9] Angel X Chang, Thomas Funkhouser, Leonidas Guibas, Pat Hanrahan, Qixing Huang, Zimo Li, Silvio Savarese, Manolis Savva, Shuran Song, Hao Su, et al. Shapenet: An information-rich 3d model repository. *arXiv preprint*, 2015.
- [10] Anpei Chen, Zexiang Xu, Andreas Geiger, Jingyi Yu, and Hao Su. Tensorf: Tensorial radiance fields. In *ECCV*, pages 333–350. Springer, 2022.
- [11] Anpei Chen, Zexiang Xu, Fuqiang Zhao, Xiaoshuai Zhang, Fanbo Xiang, Jingyi Yu, and Hao Su. Mvsnerf: Fast generalizable radiance field reconstruction from multi-view stereo. In *ICCV*, pages 14124–14133, 2021.
- [12] Dave Zhenyu Chen, Yawar Siddiqui, Hsin-Ying Lee, Sergey Tulyakov, and Matthias Nießner. Text2tex: Text-driven texture synthesis via diffusion models. *arXiv preprint*, 2023.
- [13] Xi Chen, Yan Duan, Rein Houthoofd, John Schulman, Ilya Sutskever, and Pieter Abbeel. Infogan: Interpretable representation learning by information maximizing generative adversarial nets. *NeurIPS*, 29, 2016.
- [14] An-Chieh Cheng, Xueting Li, Sifei Liu, Min Sun, and Ming-Hsuan Yang. Autoregressive 3d shape generation via canonical mapping. In *ECCV*, pages 89–104. Springer, 2022.
- [15] An-Chieh Cheng, Xueting Li, Min Sun, Ming-Hsuan Yang, and Sifei Liu. Learning 3d dense correspondence via canonical point autoencoder. *NeurIPS*, 34:6608–6620, 2021.
- [16] George R Cross and Anil K Jain. Markov random field texture models. *PAMI*, pages 25–39, 1983.
- [17] Angela Dai, Yawar Siddiqui, Justus Thies, Julien Valentin, and Matthias Nießner. Spsg: Self-supervised photometric scene generation from rgb-d scans. In *CVPR*, pages 1747–1756, 2021.
- [18] Robert A Drebin, Loren Carpenter, and Pat Hanrahan. Volume rendering. *SIGGRAPH*, 22(4):65–74, 1988.
- [19] Vincent Dumoulin, Ishmael Belghazi, Ben Poole, Olivier Mastroiello, Alex Lamb, Martin Arjovsky, and Aaron Courville. Adversarially learned inference. *arXiv preprint*, 2016.
- [20] Alexei A Efros and William T Freeman. Image quilting for texture synthesis and transfer. In *SIGGRAPH*, pages 341–346, 2001.
- [21] Alexei A Efros and Thomas K Leung. Texture synthesis by non-parametric sampling. In *ICCV*, volume 2, pages 1033–1038. IEEE, 1999.
- [22] Simone Foti, Bongjin Koo, Danail Stoyanov, and Matthew J Clarkson. 3d shape variational autoencoder latent disentanglement via mini-batch feature swapping for bodies and faces. In *CVPR*, pages 18730–18739, 2022.
- [23] Jun Gao, Tianchang Shen, Zian Wang, Wenzheng Chen, Kangxue Yin, Daiqing Li, Or Litany, Zan Gojcic, and Sanja Fidler. Get3d: A generative model of high quality 3d textured shapes learned from images. In *NeurIPS*, 2022.
- [24] Ian Goodfellow, Jean Pouget-Abadie, Mehdi Mirza, Bing Xu, David Warde-Farley, Sherjil Ozair, Aaron Courville, and Yoshua Bengio. Generative adversarial networks. In *NeurIPS*, volume 27, 2014.
- [25] Philipp Henzler, Niloy J Mitra, and Tobias Ritschel. Learning a neural 3d texture space from 2d exemplars. In *CVPR*, pages 8356–8364, 2020.
- [26] Tao Hu, Shu Liu, Yilun Chen, Tiancheng Shen, and Jiaya Jia. Efficientnerf efficient neural radiance fields. In *CVPR*, pages 12902–12911, 2022.

- [27] Xun Huang, Ming-Yu Liu, Serge Belongie, and Jan Kautz. Multimodal unsupervised image-to-image translation. In *ECCV*, pages 172–189, 2018.
- [28] Ananya Harsh Jha, Saket Anand, Maneesh Singh, and VSR Veeravasarapu. Disentangling factors of variation with cycle-consistent variational auto-encoders. In *ECCV*, pages 805–820, 2018.
- [29] Tero Karras, Miika Aittala, Janne Hellsten, Samuli Laine, Jaakko Lehtinen, and Timo Aila. Training generative adversarial networks with limited data. *NeurIPS*, 33:12104–12114, 2020.
- [30] Tero Karras, Samuli Laine, and Timo Aila. A style-based generator architecture for generative adversarial networks. In *CVPR*, pages 4401–4410, 2019.
- [31] Tero Karras, Samuli Laine, Miika Aittala, Janne Hellsten, Jaakko Lehtinen, and Timo Aila. Analyzing and improving the image quality of stylegan. In *CVPR*, pages 8110–8119, 2020.
- [32] Diederik P Kingma and Max Welling. Auto-encoding variational bayes. *arXiv preprint*, 2013.
- [33] Johannes Kopf, Chi-Wing Fu, Daniel Cohen-Or, Oliver Deussen, Dani Lischinski, and Tien-Tsin Wong. Solid texture synthesis from 2d exemplars. In *SIGGRAPH*, 2007.
- [34] Tejas D Kulkarni, William F Whitney, Pushmeet Kohli, and Josh Tenenbaum. Deep convolutional inverse graphics network. *NeurIPS*, 28, 2015.
- [35] Jiaxin Li, Zijian Feng, Qi She, Henghui Ding, Changhu Wang, and Gim Hee Lee. Mine: Towards continuous depth mpi with nerf for novel view synthesis. In *ICCV*, pages 12578–12588, 2021.
- [36] Ruihui Li, Xianzhi Li, Ka-Hei Hui, and Chi-Wing Fu. Srgan: Sphere-guided 3d shape generation and manipulation. *TOG*, 40(4):1–12, 2021.
- [37] Lin Liang, Ce Liu, Ying-Qing Xu, Baining Guo, and Heung-Yeung Shum. Real-time texture synthesis by patch-based sampling. *TOG*, 20(3):127–150, 2001.
- [38] Andrew Liu, Shiry Ginosar, Tinghui Zhou, Alexei A Efros, and Noah Snavely. Learning to factorize and relight a city. In *ECCV*, pages 544–561. Springer, 2020.
- [39] Shichen Liu, Tianye Li, Weikai Chen, and Hao Li. Soft rasterizer: A differentiable renderer for image-based 3d reasoning. *ICCV*, Oct 2019.
- [40] Ricardo Martin-Brualla, Noha Radwan, Mehdi SM Sajjadi, Jonathan T Barron, Alexey Dosovitskiy, and Daniel Duckworth. Nerf in the wild: Neural radiance fields for unconstrained photo collections. In *CVPR*, pages 7210–7219, 2021.
- [41] Emile Mathieu, Tom Rainforth, Nana Siddharth, and Yee Whye Teh. Disentangling disentanglement in variational autoencoders. In *ICML*, pages 4402–4412. PMLR, 2019.
- [42] Ben Mildenhall, Pratul P. Srinivasan, Matthew Tancik, Jonathan T. Barron, Ravi Ramamoorthi, and Ren Ng. Nerf: Representing scenes as neural radiance fields for view synthesis. In *ECCV*, 2020.
- [43] Jiteng Mu, Shalini De Mello, Zhiding Yu, Nuno Vasconcelos, Xiaolong Wang, Jan Kautz, and Sifei Liu. Coordgan: Self-supervised dense correspondences emerge from gans. In *CVPR*, pages 10011–10020, 2022.
- [44] Thu Nguyen-Phuoc, Chuan Li, Lucas Theis, Christian Richardt, and Yong-Liang Yang. Hologan: Unsupervised learning of 3d representations from natural images. In *ICCV*, pages 7588–7597, 2019.
- [45] Michael Niemeyer, Lars Mescheder, Michael Oechsle, and Andreas Geiger. Differentiable volumetric rendering: Learning implicit 3d representations without 3d supervision. In *CVPR*, pages 3504–3515, 2020.
- [46] Michael Oechsle, Lars Mescheder, Michael Niemeyer, Thilo Strauss, and Andreas Geiger. Texture fields: Learning texture representations in function space. In *ICCV*, pages 4531–4540, 2019.
- [47] Michael Oechsle, Songyou Peng, and Andreas Geiger. Unisurf: Unifying neural implicit surfaces and radiance fields for multi-view reconstruction. In *ICCV*, pages 5589–5599, 2021.
- [48] Jonathan Palacios and Eugene Zhang. Rotational symmetry field design on surfaces. *TOG*, 26(3):55–es, 2007.
- [49] Keunhong Park, Konstantinos Rematas, Ali Farhadi, and Steven M. Seitz. Photoshape: Photorealistic materials for large-scale shape collections. *TOG*, 37(6), Nov. 2018.
- [50] Keunhong Park, Konstantinos Rematas, Ali Farhadi, and Steven M. Seitz. Photoshape: Photorealistic materials for large-scale shape collections. *TOG*, 2018.
- [51] Taesung Park, Jun-Yan Zhu, Oliver Wang, Jingwan Lu, Eli Shechtman, Alexei Efros, and Richard Zhang. Swapping autoencoder for deep image manipulation. *NeurIPS*, 33:7198–7211, 2020.
- [52] Dario Pavllo, Jonas Kohler, Thomas Hofmann, and Aurelien Lucchi. Learning generative models of textured 3d meshes from real-world images. In *ICCV*, pages 13879–13889, 2021.
- [53] Dario Pavllo, Graham Spinks, Thomas Hofmann, Marie-Francine Moens, and Aurelien Lucchi. Convolutional generation of textured 3d meshes. *NeurIPS*, 33:870–882, 2020.
- [54] Songyou Peng, Chiyu Jiang, Yiyi Liao, Michael Niemeyer, Marc Pollefeys, and Andreas Geiger. Shape as points: A differentiable poisson solver. *NeurIPS*, 34:13032–13044, 2021.
- [55] Stanislav Pidhorskyi, Donald A Adjeroh, and Gianfranco Doretto. Adversarial latent autoencoders. In *CVPR*, pages 14104–14113, 2020.
- [56] Tiziano Portenier, Siavash Arjomand Bigdeli, and Orcun Goksel. Gramgan: Deep 3d texture synthesis from 2d exemplars. *NeurIPS*, 33:6994–7004, 2020.
- [57] Amit Raj, Cusuh Ham, Connelly Barnes, Vladimir Kim, Jingwan Lu, and James Hays. Learning to generate textures on 3d meshes. In *CVPRW*, pages 32–38, 2019.
- [58] Jürgen Schmidhuber. Deep learning in neural networks: An overview. *Neural Networks*, 61:85–117, 2015.
- [59] Katja Schwarz, Yiyi Liao, Michael Niemeyer, and Andreas Geiger. Graf: Generative radiance fields for 3d-aware image synthesis. *NeurIPS*, 33:20154–20166, 2020.
- [60] Yawar Siddiqui, Justus Thies, Fangchang Ma, Qi Shan, Matthias Nießner, and Angela Dai. Texturify: Generating textures on 3d shape surfaces. In *ECCV*, pages 72–88. Springer, 2022.

- [61] Krishna Kumar Singh, Utkarsh Ojha, and Yong Jae Lee. Finegan: Unsupervised hierarchical disentanglement for fine-grained object generation and discovery. In *CVPR*, pages 6490–6499, 2019.
- [62] Ivan Skorokhodov, Sergey Tulyakov, Yiqun Wang, and Peter Wonka. Epigraf: Rethinking training of 3d gans. *NeurIPS*, 2022.
- [63] Gabriel Taubin. A signal processing approach to fair surface design. In *SIGGRAPH*, pages 351–358, 1995.
- [64] Alex Trevithick and Bo Yang. Grf: Learning a general radiance field for 3d representation and rendering. In *ICCV*, pages 15182–15192, 2021.
- [65] Greg Turk. Texture synthesis on surfaces. In *SIGGRAPH*, pages 347–354, 2001.
- [66] Naveen Venkat, Mayank Agarwal, Maneesh Singh, and Shubham Tulsiani. Geometry-biased transformers for novel view synthesis. *arXiv preprint*, 2023.
- [67] Dor Verbin, Peter Hedman, Ben Mildenhall, Todd Zickler, Jonathan T Barron, and Pratul P Srinivasan. Ref-nerf: Structured view-dependent appearance for neural radiance fields. In *CVPR*, pages 5481–5490. IEEE, 2022.
- [68] Peihao Wang, Xuxi Chen, Tianlong Chen, Subhashini Venugopalan, Zhangyang Wang, et al. Is attention all nerf needs? *arXiv preprint*, 2022.
- [69] Peng Wang, Lingjie Liu, Yuan Liu, Christian Theobalt, Taku Komura, and Wenping Wang. Neus: Learning neural implicit surfaces by volume rendering for multi-view reconstruction. *NeurIPS*, 2021.
- [70] Qianqian Wang, Zhicheng Wang, Kyle Genova, Pratul Srinivasan, Howard Zhou, Jonathan T. Barron, Ricardo Martin-Brualla, Noah Snavely, and Thomas Funkhouser. Ibrnet: Learning multi-view image-based rendering. In *CVPR*, 2021.
- [71] Yue Wang, Yongbin Sun, Ziwei Liu, Sanjay E Sarma, Michael M Bronstein, and Justin M Solomon. Dynamic graph cnn for learning on point clouds. *TOG*, 38(5):1–12, 2019.
- [72] Fanbo Xiang, Zexiang Xu, Milos Hasan, Yannick Hold-Geoffroy, Kalyan Sunkavalli, and Hao Su. Neutex: Neural texture mapping for volumetric neural rendering. In *CVPR*, pages 7119–7128, 2021.
- [73] Qiangeng Xu, Zexiang Xu, Julien Philip, Sai Bi, Zhixin Shu, Kalyan Sunkavalli, and Ulrich Neumann. Point-nerf: Point-based neural radiance fields. In *CVPR*, pages 5438–5448, 2022.
- [74] Bangbang Yang, Chong Bao, Junyi Zeng, Hujun Bao, Yinda Zhang, Zhaopeng Cui, and Guofeng Zhang. Neumesh: Learning disentangled neural mesh-based implicit field for geometry and texture editing. In *ECCV*, pages 597–614. Springer, 2022.
- [75] Linjie Yang, Ping Luo, Chen Change Loy, and Xiaoou Tang. A large-scale car dataset for fine-grained categorization and verification. In *CVPR*, pages 3973–3981, 2015.
- [76] Lior Yariv, Jiatao Gu, Yoni Kasten, and Yaron Lipman. Volume rendering of neural implicit surfaces. *NeurIPS*, 34:4805–4815, 2021.
- [77] Lior Yariv, Yoni Kasten, Dror Moran, Meirav Galun, Matan Atzmon, Basri Ronen, and Yaron Lipman. Multiview neural surface reconstruction by disentangling geometry and appearance. *NeurIPS*, 33:2492–2502, 2020.
- [78] Alex Yu, Vickie Ye, Matthew Tancik, and Angjoo Kanazawa. pixelnerf: Neural radiance fields from one or few images. In *CVPR*, pages 4578–4587, 2021.
- [79] Rui Yu, Yue Dong, Pieter Peers, and Xin Tong. Learning texture generators for 3d shape collections from internet photo sets. In *BMVC*, 2021.
- [80] Xiaohui Zeng, Arash Vahdat, Francis Williams, Zan Gojcic, Or Litany, Sanja Fidler, and Karsten Kreis. Lion: Latent point diffusion models for 3d shape generation. In *NeurIPS*, 2022.
- [81] Han Zhang, Ian Goodfellow, Dimitris Metaxas, and Augustus Odena. Self-attention generative adversarial networks. In *ICML*, pages 7354–7363. PMLR, 2019.
- [82] Jason Zhang, Gengshan Yang, Shubham Tulsiani, and Deva Ramanan. Ners: neural reflectance surfaces for sparse-view 3d reconstruction in the wild. *NeurIPS*, 34:29835–29847, 2021.

Contents

1. Introduction	2
2. Related work	2
3. Texture UV Radiance Fields	3
3.1. Canonical Surface Auto-encoder	3
3.2. Texture Feature Generator	3
3.3. Rendering from UV Sphere	4
3.4. Generative Adversarial Training	5
4. Experiments	5
4.1. Dataset	5
4.2. Baselines	5
4.3. Evaluation Metrics	6
4.4. Results	7
5. Conclusion	9
A Results	13
A.1. Qualitative Results of Texture Editing	13
A.2. Qualitative Results of High-Resolution Synthesis	14
A.3. Qualitative Results of Texture Transfer	21
B Ablation Studies	26
B.1. Ablation Study on Canonical Surface Auto-encoder	26
B.2. Ablation Study on Different UV Resolution	27
C Implementation Details	27
C.1. TUVF Rendering	27
C.2. Canonical Surface Auto-encoder	27
C.3. Texture Generator h_θ	28
C.4. Patch-based Discriminator	29
C.5. Training Details	29
D Computational Time and Model Size	29
E Limitations	30

A. Results

A.1. Qualitative Results of Texture Editing

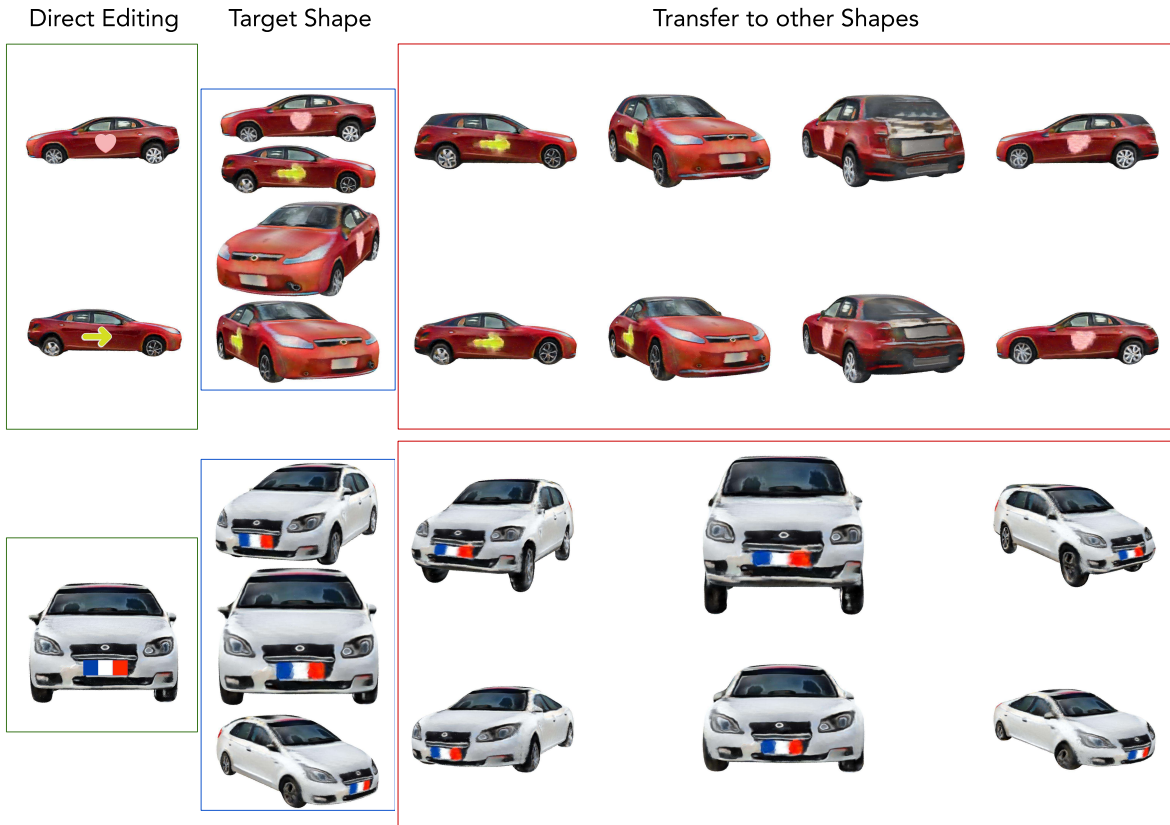


Figure 7. **Texture Editing and Transfer.** Our approach offers exceptional flexibility when it comes to texture editing. We support a range of texture editing techniques, including texture swapping, filling, and painting operations. Given a synthesized texture, one can directly operate on the rendered view to edit the texture (as illustrated by the *green box*). By fine-tuning the edited image using the back-propagation to the texture feature, we can obtain an edited texture that is 3D consistent across different views (as shown in the *blue box*). Moreover, this edited texture feature can also be transferred among different shapes (as demonstrated by the *red box*).

A.2. Qualitative Results of High-Resolution Synthesis



Figure 8. **Our results on Compcars dataset.** The model is trained with 512×512 resolution, images shown are rendered with 1024×1024 resolution. Compared to Texturify [60] (results shown in Figure 11 and Figure 12), our texture synthesis approach produces textures with superior detail. Notably, our generator is capable of synthesizing intricate features such as *logos*, *door handles*, *car wipers*, and *wheel frames*. Zoom in for the best viewing.



Figure 9. **Our results on Compcars dataset.** The model is trained with 512×512 resolution, images shown are rendered with 1024×1024 resolution. Note that all the images are rendered from the same instance, including images in Figure 8 and Figure 10. This highlights the effectiveness of our proposed method in synthesizing photo-realistic textures while maintaining 3D consistency. Zoom in for the best viewing.



Figure 10. **Our results on Compcars dataset.** The model is trained with 512×512 resolution, images shown are rendered with 1024×1024 resolution. In addition to generating different global colors, our proposed method can generate diverse textures by including intricate local details. For example, the generated textures may include *unique logos* (different from those shown in Figure 9) or *distinct tail light styles* (different from Figure 8). Zoom in for the best viewing.



Figure 11. **Texturify [60] results on Compcars dataset.** The model is trained with 512×512 resolution, images shown are rendered with 1024×1024 resolution. The sample shown in this figure was generated using the pre-trained model provided by the authors. Notably, all the images in this figure depict different render angles of the same instance.



Figure 12. **Texturify [60] results on Compcars dataset.** The model is trained with 512×512 resolution, images shown are rendered with 1024×1024 resolution. The sample shown in this figure was generated using the pre-trained model provided by the authors. Notably, all the images in this figure depict different render angles of the same instance.



Figure 13. **Our results on Photoshape dataset.** The model is trained with 512×512 resolution, images shown are rendered with 1024×1024 resolution. Our model is highly effective in synthesizing top-quality textures for chairs. Interestingly, the generated textures may even feature a variety of material styles, such as *black leather*, *suede fabric*, or *flannel* (see Figure 14), adding an extra level of realism to the textures. Zoom in for the best viewing.



Figure 14. **Our results on Photoshape dataset.** The model is trained with 512×512 resolution, images shown are rendered with 1024×1024 resolution. Thanks to the correspondence learned from our Canonical Surface Auto-encoder, textures can be generated without interference from geometry information. Furthermore, the model can predict accurate textures for different parts of the object. For instance, the legs of the chair may have distinct textures from the seats, and the boundary between these two parts is clearly defined. This demonstrates the importance of the correspondence learned from the Canonical Surface Auto-encoder. Zoom in for the best viewing.

A.3. Qualitative Results of Texture Transfer

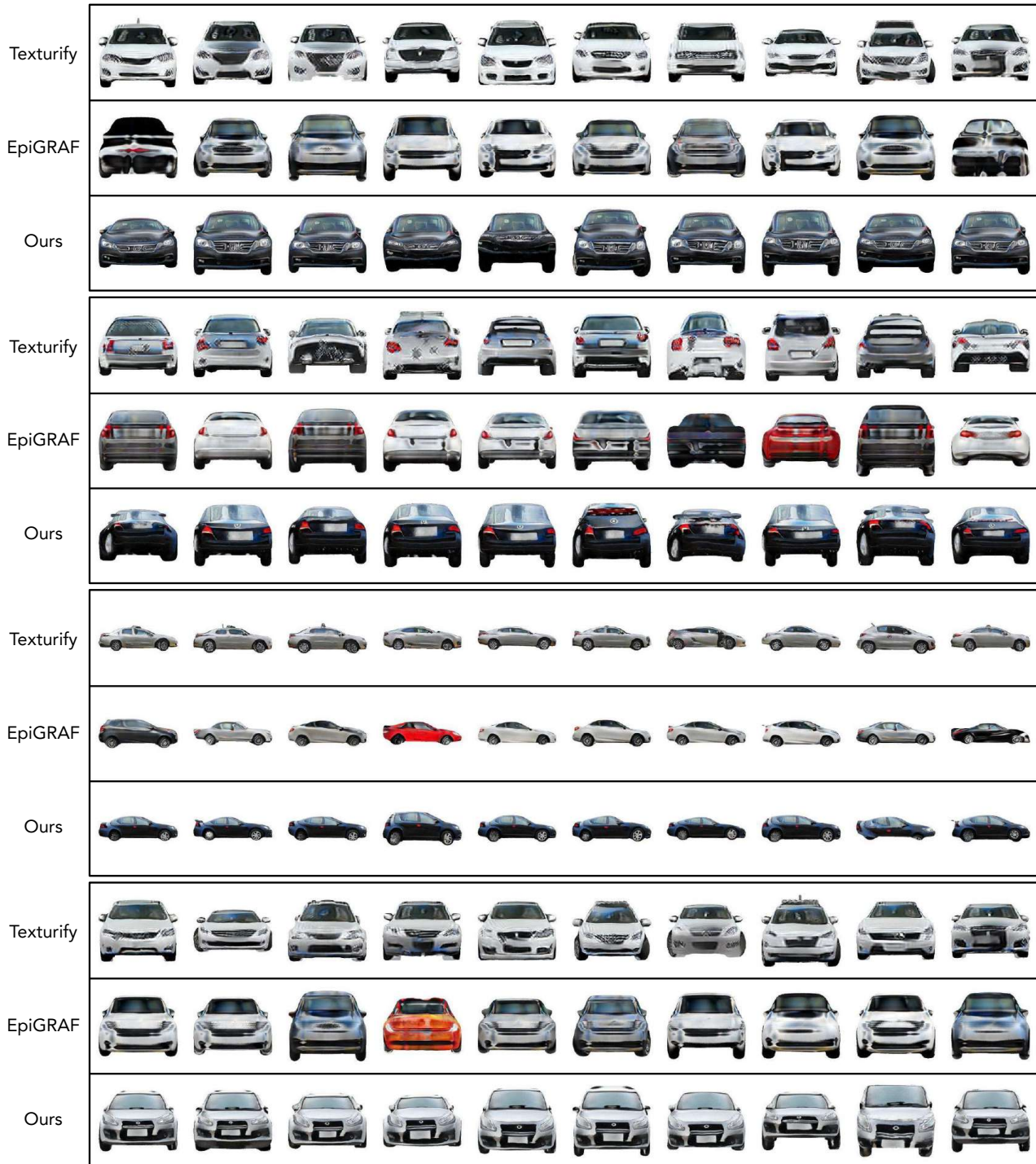


Figure 15. **Texture Transfer Results on CompCars dataset.** Each approach (in the same row) applies the same texture code to synthesize textures on different input shapes. Our method can generate textures that exhibit consistency across all shapes, unlike other approaches (e.g., Texturify [60] and EpiGRAF [62]), which may produce different styles or local details on different object shapes even when using the same texture code.

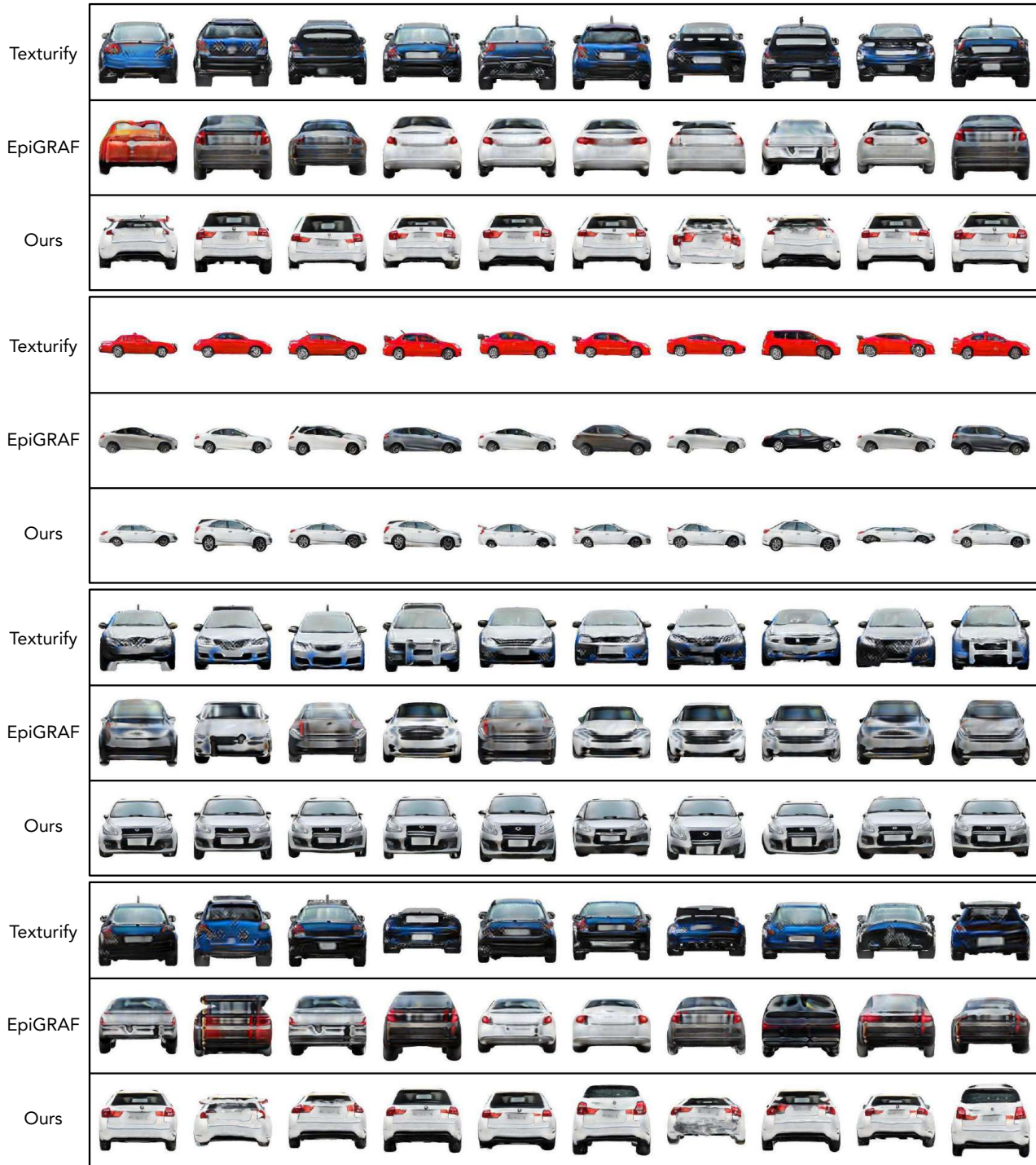


Figure 16. **Texture Transfer Results on CompCars dataset.** Each approach (in the same row) applies the same texture code to synthesize textures on different input shapes. Our method can generate textures that exhibit consistency across all shapes, unlike other approaches (e.g., Texturify [60] and EpiGRAF [62]), which may produce different styles or local details on different object shapes even when using the same texture code. Consider the results shown in row 4 of the figure. While the samples generated by the Texturify [60] method exhibit consistency in global color (i.e., all the cars are red), the same texture code may result in different window styles (i.e., number of windows).

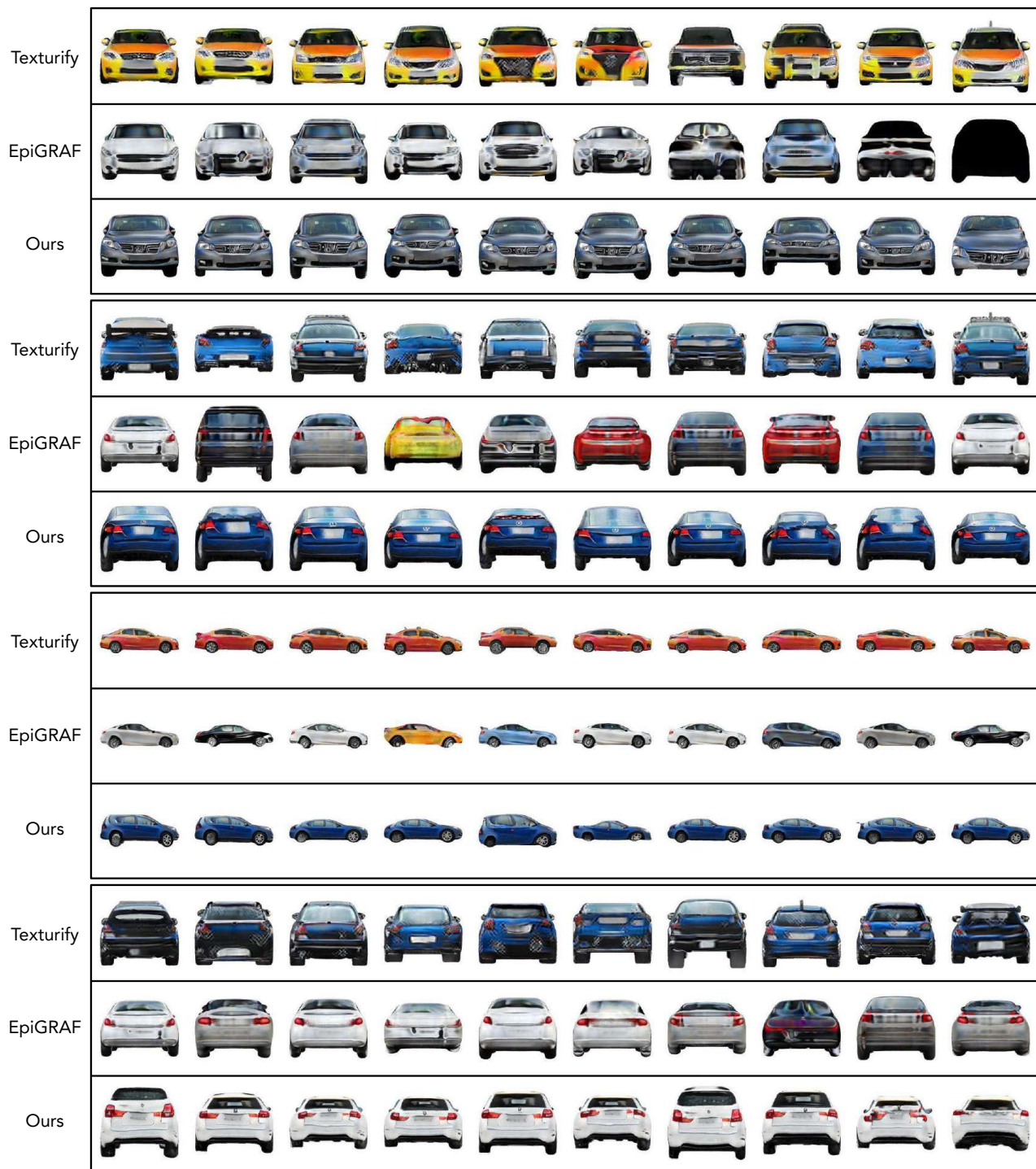


Figure 17. **Texture Transfer Results on CompCars dataset.** Each approach (in the same row) applies the same texture code to synthesize textures on different input shapes. Our method can generate textures that exhibit consistency across all shapes, unlike other approaches (e.g., Texturify [60] and EpiGRAF [62]), which may produce different styles or local details on different object shapes even when using the same texture code.



Figure 18. **Texture Transfer Results on Photoshape dataset.** Each approach (in the same row) applies the same texture code to synthesize textures on different input shapes. Our method can generate textures that exhibit consistency across all shapes, unlike other approaches (e.g., Texturify [60] and EpiGRAF [62]), which may produce different styles or local details on different object shapes even when using the same texture code.

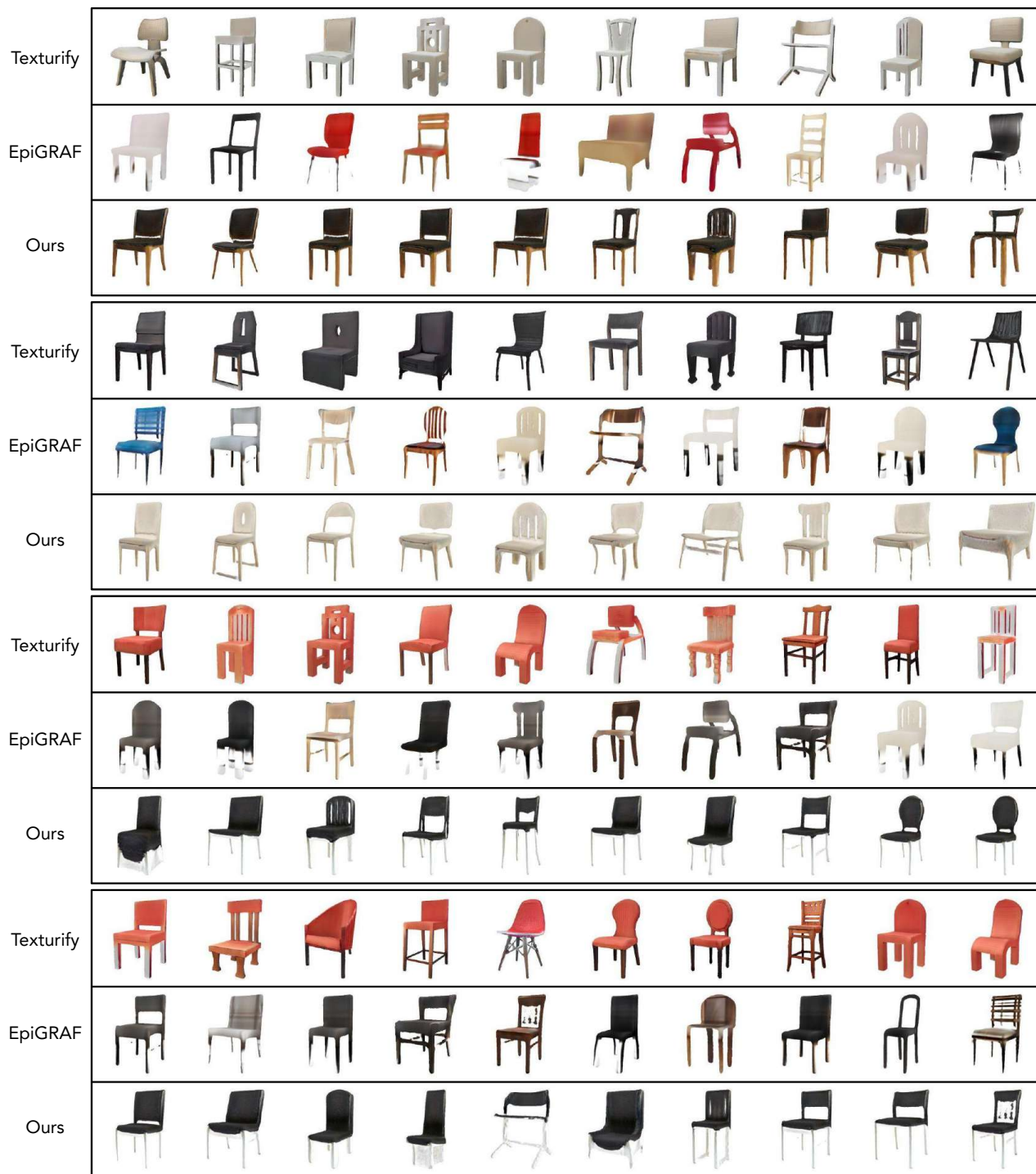


Figure 19. **Texture Transfer Results on Photoshape dataset.** Each approach (in the same row) applies the same texture code to synthesize textures on different input shapes. Our method can generate textures that exhibit consistency across all shapes, unlike other approaches (e.g., Texturify [60] and EpiGRAF [62]), which may produce different styles or local details on different object shapes even when using the same texture code.

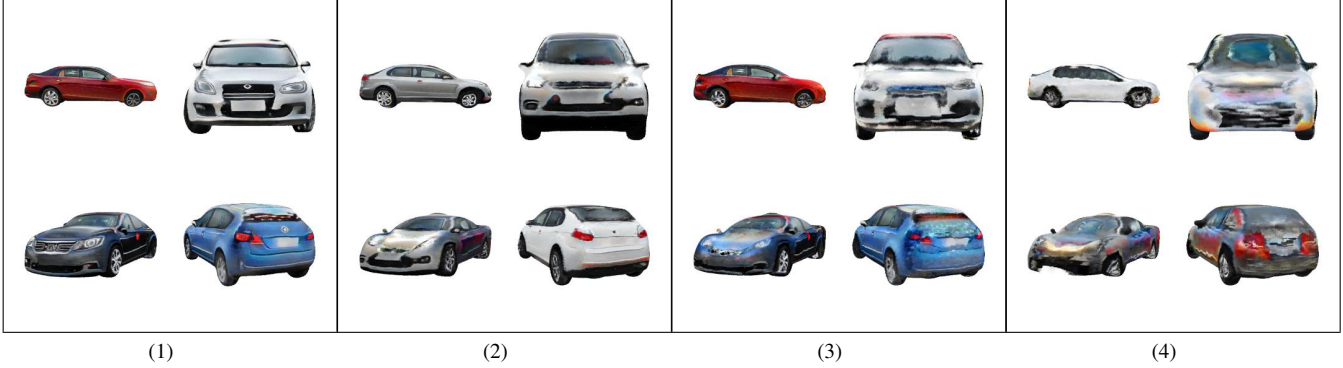


Figure 20. Visualization of the ablation study over the Canonical Surface Auto-encoder. The four sub-figures correspond to the four settings from left to right. Please zoom in for the best viewing.

B. Ablation Studies

B.1. Ablation Study on Canonical Surface Auto-encoder

Method	Mapping Direction	GT Geometry	Proxyless Surface	Smoothness	FID ↓	KID ↓
1 (<i>base</i>)	UV → Surface		✓	✓	41.79	2.95
2	UV → Surface	✓		✓	61.81	4.08
3	UV → Surface	✓	✓		79.43	6.16
4	Surface → UV	✓	✓		139.19	12.92

Table 5. Ablation Study over Canonical Surface Auto-encoder. Evaluated on the CompCars dataset.

One drawback of our framework is that the auto-encoded indicator grid may not be perfect. As a result, we investigated several different network designs for the stage-1 geometry pre-training, which enabled us to learn texture synthesis using the ground-truth indicator function. We considered comparing four settings in this study:

1. *Our Canonical Surface Auto-encoder*. The geometry network takes UV points as inputs and maps them to the surface. An additional function g_θ is learned to predict the surface normal for each point, and an auto-encoded indicator function is obtained. Texture synthesis is performed using the auto-encoded indicator function.
2. The geometry network takes UV points as inputs and maps them to the surface. No g_θ is used. Texture synthesis is performed using the ground-truth indicator function.
3. The geometry network takes UV points as inputs and maps them to the surface. No g_θ is used. Texture synthesis uses the ground-truth indicator function, while points are warped to the ground-truth surface via the nearest neighbor.
4. The geometry network takes surface points as inputs and maps them to the UV. In this case, there is no need for g_θ , and texture synthesis is learned using the ground-truth indicator function.

Two important factors may affect the quality of synthesis. First, the surface points should lie as close to the exact surface of the indicator function as possible. This is because our MLP_F takes the nearest neighbor feature and the distance between the query point and the nearest neighbor as inputs. If there is a gap between the points and the surface of the indicator function, it can confuse MLP_F and harm the performance. Secondly, the surface points should be as smooth as possible, i.e., evenly distributed among the surface. This ensures that each surface point contributes to a similar amount of surface area. The results of our ablation study on the car category can be found in Table 5. We also show samples from each setting in Figure 20. The results obtained for settings without smooth correspondence (e.g., setting 3 and 4) show that the textures are more blurry and tend to have distortions. On the other hand, our method produces sharper details compared to setting 2, which is trained on proxy surface points. This study demonstrates the unique advantage of our Canonical Surface Auto-encoder design, in which

we can learn UV-to-surface mapping with smooth correspondence. Therefore, learning an additional function g_θ to predict point normal and obtain an auto-encoded indicator function is necessary to obtain high-fidelity textures.

B.2. Ablation Study on Different UV Resolution

UV Resolution	FID ↓	KID ↓
2K (<i>base</i>)	41.79	2.95
1K	43.65	3.01

Table 6. Ablation Study over different UV resolution. Evaluated on the CompCars dataset.

We investigated the effect of UV resolution on the quality of our method. To achieve this, we compared our base method with different numbers of UV resolution (1K and 2K). The results in Table 6 showed that increasing the UV resolution leads to improved performance in terms of producing higher-quality fine-scale details. However, we found that using level 4 ico-sphere vertices (i.e., 2K points) is sufficient to achieve high-quality results. Further increasing the resolution would result in prohibitively long training times due to the K nearest neighbor search. For example, using level 5 ico-sphere vertices would result in 10242 points, which would significantly slow down the training speed.

C. Implementation Details

C.1. TUVF Rendering

To obtain samples from the UV sphere, we use the vertices of a level 4 ico-sphere, which provides us with 2562 coordinates. After passing these coordinates through the mapping functions f_θ , g_θ , and h_θ , we obtain 2562 surface points ($X_{p'}$), 2562 surface normal ($N_{p'}$), a 128^3 indication function grid (χ'), and 2562 32-dimensional texture feature vectors. To compute the final color of a ray, we first sample 256 shading points and identify the valid points using the indication function grid χ' . Next, we sample three valid shading points around the surface, and for each valid shading location x_i , we conduct a K-nearest neighbor search on the surface points $X_{p'}$. We perform spatial interpolation of the texture feature on the K-nearest surface points to obtain the texture feature c_{x_i} for the current shading points x_i . In our experiment, we set K to 4, which is not computationally expensive since we only deal with 2562 surface points.

C.2. Canonical Surface Auto-encoder

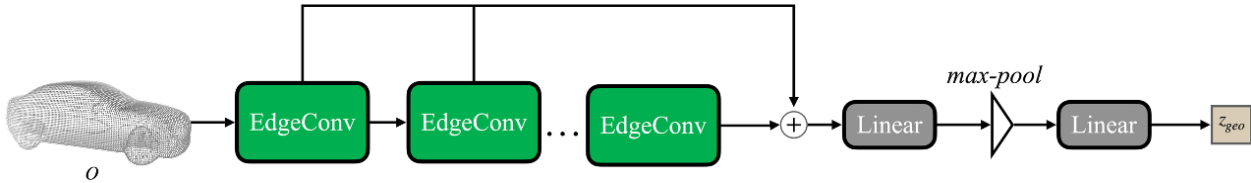


Figure 21. Architecture of our Shape Encoder \mathcal{E} .

Shape Encoder \mathcal{E} . Given a 3D object O , we first normalize the object to a unit cube and sample 4096 points on the surface as inputs to the Shape Encoder \mathcal{E} [15]. The encoder structure is adopted from DGCNN [71], which contains 3 EdgeConv layers using neighborhood size 20. The output of the encoder is a global shape latent $z_{geo} \in R^d$ where $d = 256$.

Surface Points Decoder f_θ and g_θ . Both the surface points decoder f_θ and surface normal decoder g_θ share the same decoder architecture, which is adapted from [14]. We show the detailed architecture of our decoder in Figure 22. The decoder architecture takes a set of point coordinates X_{in} and geometry feature z_{geo} as input and learns to output a set of point coordinates X_{out} in a point-wise manner. To process a set of point coordinates X_{in} and geometry feature z_{geo} , the decoder first creates a matrix by duplicating z_{geo} for each coordinate in X_{in} and concatenating it to each coordinate. This matrix includes both the point coordinates and geometry features. The decoder has two branches: one branch uses an EdgeConv [71] with an attention module to extract point-wise spatial features from the point coordinates. The attention

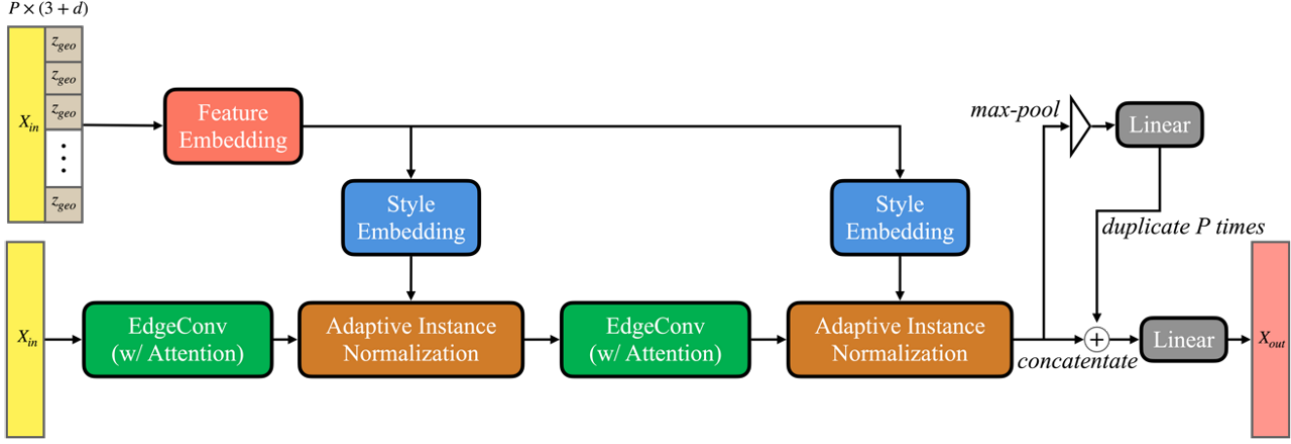


Figure 22. Architecture of our Surface Points Decoder f_θ and Surface Normal Decoder g_θ .

module is adopted from [36], which regresses additional weights among the K point neighbors' features as attentions. The other branch employs a nonlinear feature embedding technique to extract style features from the geometry feature. The local styles are then combined with the spatial features using adaptive instance normalization [19] to create fused features. The style embedding and fusion process is repeated, and finally, the fused feature is used to predict the final output X_{out} . It is worth noting that both the surface points decoder f_θ and surface normal decoder g_θ use the same geometric features as input. However, they differ in their coordinate input. Specifically, f_θ takes 2562 UV coordinates as input, while g_θ uses the 2562 output coordinates from f_θ as input.

C.3. Texture Generator h_θ

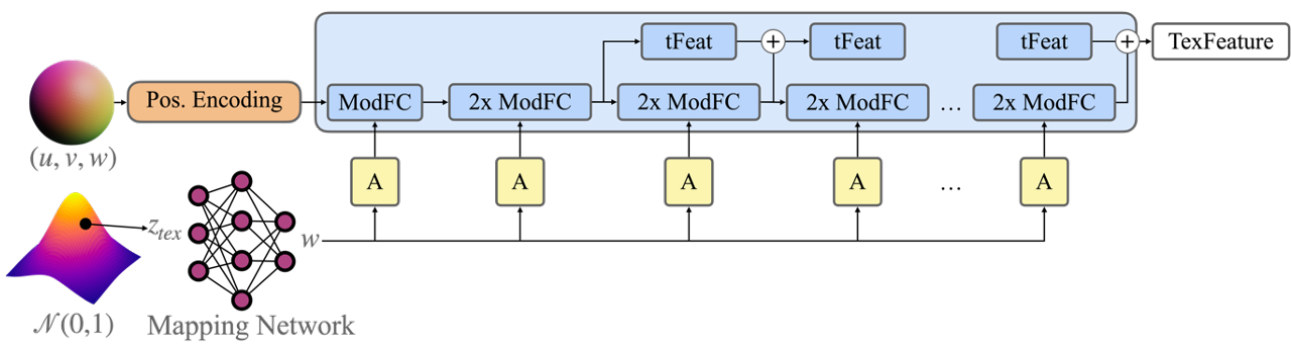


Figure 23. Architecture of our UV texture feature generator h_θ . A denotes the Affine Transformation module [30], ModFC denotes modulated fully connected layers, and tFeat denotes temporary features.

Our generator network, which has a multi-layer perceptron-type architecture [1], is capable of synthesizing texture features on a UV sphere. To achieve this, we use a random texture latent vector z_{tex} that is shared across all UV coordinates, as well as the UV coordinates (u, v, w) as input. The generator then returns the 32-dim texture feature vector value c for that particular UV coordinate. Thus, to compute the entire UV sphere, the generator is evaluated at every pair of coordinates (u, v, w) while keeping the texture latent vector z_{tex} fixed. Specifically, we utilize a mapping network to convert the random texture latent vector z_{tex} into a style vector with the same dimension as z_{tex} . This vector injects style into the generation process through weight modulation. We follow the Fourier positional encoding method outlined in [1] to encode the input UV coordinates. The resulting coordinate features pass through the modulated fully connected layers (ModFC), which are controlled by the style vector mentioned above. Finally, we obtain a 32-dimensional texture feature for the input coordinate.

C.4. Patch-based Discriminator

Our discriminator is based on EpiGRAF [62], which is similar to the one used in StyleGAN2 [31], but modulated by the patch location and scale parameters. We follow the patch-wise optimization approach for training, along with using Beta distribution [62] for sampling the scale. We use an initial beta value of $1e^{-4}$ and gradually anneal it to 0.8 after processing $1e^7$ images.

C.5. Training Details

Algorithm 1 : The training phase of our approach consists of two stages: (1) Canonical Surface Auto-encoder (2) Texture Feature Generator using adversarial objectives

(A) CANONICAL SURFACE AUTO-ENCODER

▷ 12 hours on ShapeNet Car dataset

- 1: Sub-sample points from the input point clouds as x and the canonical UV sphere π ;
 - 2: Compute ground-truth indicator function grid χ ;
 - 3: Initialize weights of the encoder \mathcal{E} , decoder f_θ and g_θ ;
 - 4: **while** not converged **do**
 - 5: **foreach** iteration **do**
 - 6: $z_{geo} \leftarrow \mathcal{E}(x)$;
 - 7: $\hat{x} \leftarrow f_\theta([\pi_i, z_{geo}])$, where $\pi_i \in \pi$;
 - 8: $\hat{n} \leftarrow g_\theta([\hat{x}_i, z_{geo}])$, where $\hat{x}_i \in \hat{x}$;
 - 9: $\chi' \leftarrow d_{psr}(\hat{x}, \hat{n})$;
 - 10: Obtain reconstruction loss $L_{CD}(\hat{x}, x)$ and $L_{DPSR}(\chi', \chi)$;
 - 11: Update weight;
-

(B) TEXTURE FEATURE GENERATOR

▷ 36 hours on CompCars dataset

- 1: Sample points from the canonical sphere π ;
 - 2: Random sample shapes with point cloud x and images from dataset I_{real} ;
 - 3: Load pre-trained encoder \mathcal{E} , f_θ and g_θ ;
 - 4: Initialize weights of the texture feature generator h_θ and patch-based discriminator D;
 - 5: **while** not converged **do**
 - 6: **foreach** iteration **do**
 - 7: Obtain \hat{x} , \hat{n} , and χ' with encoder \mathcal{E} , f_θ and g_θ ;
 - 8: Sample z_{tex} from multivariate normal distribution;
 - 9: $c_i \leftarrow h_\theta(\pi_i, z_{tex})$, where $\pi_i \in \pi$;
 - 10: $I_{fake} \leftarrow \mathcal{R}(\hat{x}, c, \chi', d)$, where \mathcal{R} denotes renderer and d are camera angles;
 - 11: Obtain loss $L_{GAN}(I_{fake}, I_{real})$;
 - 12: Update weight;
-

To demonstrate the training pipeline, we use the car category in ShapeNet and the CompCars dataset as examples. All experiments are performed on a workstation equipped with an AMD EPYC 7542 32-Core Processor (2.90GHz) and 8 Nvidia RTX 3090 TI GPUs (24GB each). We implement our framework using PyTorch 1.10. For further details and training time for each stage, please refer to Algorithm 1. *The source code will be released to the public upon publication.*

D. Computational Time and Model Size

Method	Representation	Feature Parameterization	Model Size ↓	Inference Time ↓
Texturify [60]	Mesh	24K Faces	52M	0.2039
EpiGRAF [62]	NeRF	128×128 Triplanes	31M	0.2537
Ours	NeRF	2K Point Clouds	9M	0.3806

Table 7. **The parameter size and inference time for different models.** Inference time is measured in seconds.



(1) Fail to reconstruct fine details with complex topology.

(2) Incorrect correspondences near part boundaries.

Figure 24. **Visualization of failure cases of our method.**

We provide a comparison of the inference time and model size of different models in Table 7. Specifically, we measure the inference time and size of each model based on the time and number of parameters required to generate a texture for a given shape instance and render an image of resolution 1024. All experiments are conducted on a workstation with an Intel(R) Core(TM) i7-12700K (5.00GHz) processor and a single NVIDIA RTX 3090 TI GPU (24GB). Texturify is a mesh-based approach and is more efficient in terms of rendering compared to NeRF-based methods. However, its feature space is heavily parameterized on the faces, which makes it memory inefficient. Similarly, EpiGRAF requires computing high-resolution triplanes, making it memory intensive. In contrast, we only parametrize on 2K point clouds throughout all the experiments and can achieve comparable or even better fidelity. Note that we use the same rendering approach for both our method and EpiGRAF; therefore, EpiGRAF has a lower inference time than our approach because it does not require KNN computation.

E. Limitations

Our work has some limitations inherited from [15] since our Canonical Surface Auto-encoder follows similar principles. Specifically, encoding the shape information of a point cloud in a global vector may cause fine details, such as corners and edges, to be blurred or holes to disappear after reconstruction. Similar to [15], we also observed that the correspondences predicted near holes or the boundaries between parts might be incorrect, possibly due to the sparsity nature of point clouds and the limitations of the Chamfer distance. Future research should address these limitations.